



Cite this: *Lab Chip*, 2026, **26**, 494

## Magnetophoretic long jump of magnetic microparticles in an engineered magnetic stray field landscape for highly localized and large throughput on-chip fractionation

Rico Huhnstock, <sup>a,b</sup> Lukas Paetzold, <sup>a</sup> Piotr Kuświk <sup>c</sup> and Arno Ehresmann <sup>a,b</sup>

A common issue faced by magnetic particle-based lab-on-a-chip systems, *e.g.*, for medical diagnostics, is the intrinsic fabrication-related polydispersity in particle sizes and magnetic properties. Therefore, to reduce this variation, it is prudent to integrate a pre-separation procedure for the particles into the overall workflow of the system. In this work, a concept for the controlled on-chip fractionation of micron-sized superparamagnetic beads (SPBs) is introduced, which is applicable for sorting magnetic particles according to their properties in a continuous operation mode. A specifically designed magnetic domain pattern is imprinted into an exchange-biased thin film system to generate a tailored magnetic stray field landscape (MFL), enabling lateral transport of SPBs when superposing the MFL with external magnetic field pulses. The domain pattern consists of parallel stripes with gradually increasing and decreasing width, resulting in a step-wise jumping motion of SPBs with increasing/decreasing jump distance. SPBs with different magnetophoretic mobilities, determined, among others, by the particle size and magnetic susceptibility, discontinue their lateral motion at different jump distances, *i.e.*, different lateral positions on the substrate. Thorough analysis of the motion using optical microscopy and particle tracking revealed that an increasing stripe width not only leads to a larger jump distance but also to a lowered jump velocity. As a consequence, particles are spatially separated according to their magnetic and structural properties with a large throughput and time efficiency, as simultaneous sorting occurs for all particles present on the substrate using a constant sequence of short external field pulses.

Received 27th October 2025,  
Accepted 15th December 2025

DOI: 10.1039/d5lc01000d

rsc.li/loc

### 1 Introduction

Lab-on-a-chip (LOC) platforms or miniaturized total chemical analysis systems ( $\mu$ -TAS) are considered key technologies for the implementation of rapid and cost-effective point-of-care sensing and diagnostics.<sup>1–3</sup> Existing solutions, like commonly used membrane-based lateral flow assays, are indeed cheaply produced devices; however, they come with drawbacks regarding sensitivity and reliability.<sup>4–6</sup> As a possibility for improvement, magnetic particles (MPs) in the size range of nanometers to micrometers are proposed as analytic probes.<sup>7–10</sup> Their surface properties are tunable *via* various chemical synthesis routes, offering substantial flexibility in terms of

recognizing different analyte substances<sup>11–16</sup> and their magnetic characteristics can be exploited for a controlled actuation inside applied magnetic fields. If a batch of spherical MPs shall be used on-chip, which is the typical application scenario, it is desirable that their magnetic field responses, leading to a certain motion velocity, do not differ too much, *i.e.*, fall in a narrow range around an average value. The decisive quantity for magnetic field-controlled motion of spherical MPs in liquids is their magnetophoretic mobility  $U_m$ , defined as

$$U_m = \frac{\Delta\chi V}{6\pi\eta R}, \quad (1)$$

where  $\Delta\chi$  is the difference between the magnetic susceptibilities of MP and the surrounding liquid,  $V$  is the volume of the MP,  $\eta$  is the viscosity of the liquid and  $R$  is the radius of the MP.<sup>17,18</sup>

$U_m$ , therefore, depends on the effective MP size, the MP magnetic response to an applied magnetic field and the properties of the surrounding liquid. For a given liquid, the first two parameters may vary independently among the different MPs. Typically, for all MP batches, either commercially available or lab fabricated, exact sizes and magnetic susceptibilities are challenging to control in the fabrication process and, thus, may

<sup>a</sup> Institute of Physics and Center for Interdisciplinary Nanostructure Science and Technology (CINSaT), University of Kassel, Heinrich-Plett-Str. 40, D-34132 Kassel, Germany. E-mail: rico.huhnstock@physik.uni-kassel.de

<sup>b</sup> Artificial Intelligence Methods for Experiment Design (AIM-ED), Joint Lab of Helmholtzzentrum für Materialien und Energie, Berlin (HZB) and University of Kassel, Hahn Meitner-Platz 1, D-14109 Berlin, Germany

<sup>c</sup> Institute of Molecular Physics, Polish Academy of Sciences, M. Smoluchowskiego 17, Poznań, 60-179, Poland

differ considerably. For defined on-chip functionalities, a presorting of MPs with respect to  $U_m$  is, therefore, a necessity. One concept to achieve such presorting is to use stepwise or ratchet-like MP motion technologies, where static magnetic field landscapes (MFLs) emerging from topographic micromagnetic structures on a surface<sup>19–21</sup> or stable magnetic

domain patterns in flat films<sup>22–24</sup> are superposed by a time-varying external magnetic field. The MFLs contain large magnetic field gradients over micron-sized distances, resulting in comparably strong magnetic forces exerted onto the MPs. By dynamically transforming the field gradients *via* the superposed external field, a remote-controlled, directed MP motion close to

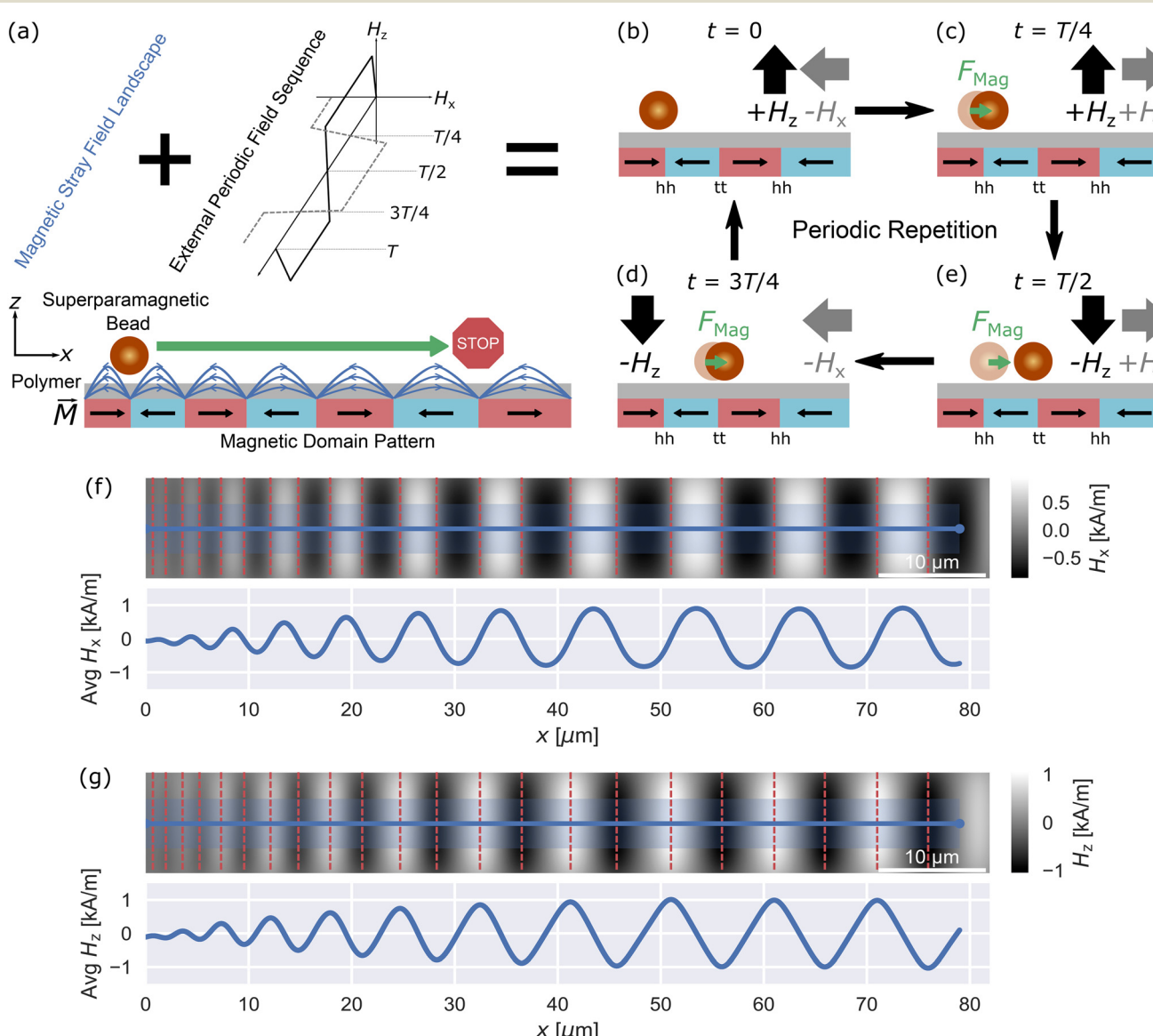


**Fig. 1** Schematic concept for the directed transport of superparamagnetic beads (SPBs) in a microfluidic environment above a magnetic stripe domain pattern with gradually increasing stripe width and a head-to-head (hh)/tail-to-tail (tt) magnetization configuration. This concept can be utilized for the mobility-dependent fractionation of SPBs based on a spatially localized immobilization when approaching larger stripe domain widths. (a) A tailored magnetic stray field landscape (MFL) is emerging from the domain pattern (dark blue lines), trapping the SPBs above stripe boundary (domain wall) positions due to a local maximum stray field strength. A periodic sequence of trapezoidal magnetic field pulses in the vertical  $z$ -direction (solid, black line) and the lateral  $x$ -direction (grey, dashed line) with a fixed alteration frequency is applied to induce SPB transport in the lateral  $x$ -direction. The external fields are superposing the MFL, resulting in a dynamic magnetic force  $F_{\text{Mag}}(x, z, t)$  acting on the particles as depicted in (b) to (e). SPBs are attracted to a position of maximum effective field strength, *i.e.*, minimum potential energy, which is shifted constantly by the externally applied field pulses, leading to near-surface, stepwise motion of the SPBs. (f and g) Computed spatial distributions of the MFL components  $H_x$  and  $H_z$  emerging from a portion of the magnetic domain pattern that was used in SPB transport experiments. Red dashed lines indicate domain wall locations. The field distributions were derived from micromagnetic simulations for a distance of 2500 nm above the patterned magnetic thin film system. A line profile visualizes the lateral evolution of the respective stray field component, averaged over the blue-shaded area.

the chip surface in a quiescent liquid is obtained, allowing for the implementation of various LOC functionalities.<sup>14,23,25–29</sup> When applying trapezoidal field pulses,<sup>23</sup> given that the pulse length extends long enough in time, the MPs start to accelerate, reach their steady-state velocity during the pulse plateau, and slow down when reaching a neighboring position of minimal potential energy. The intra-pulse (maximum) steady-state velocity  $v_{st}$  is determined by the equilibrium of accelerating magnetic force and viscous drag exerted by the surrounding fluid.<sup>23,30</sup> For sufficiently short pulses, the change of the effective field (the vector sum of the static and the external field) acting on the MP is considerably faster than the time required by the MP to reach its next position with the given  $v_{st}$ , effectively disabling a motion step for the MP. Hence, the pulse length (or pulse frequency) is a decisive experimental parameter for deciding whether MPs can follow the dynamic transformation of the effective magnetic field and, therefore, allow continuous MP motion. A higher frequency of pulses (or shorter pulse length) will only allow for motion of MPs with sufficiently large  $U_m$ , resulting in a fractionation of the MP batch according to their magnetophoretic mobilities. As this fractionation concept necessitates sweeping the external field frequency, an autonomous, continuous operation within an LOC device is not straightforward to implement.

In this work, we present a unique MFL design based on an engineered magnetic domain pattern that enables localized MP fractionation using external field pulses of constant length. In particular, we will show how ion bombardment induced magnetic patterning (IBMP) of in-plane magnetized, exchange-biased layers can be employed to fabricate parallel stripe domains with variable widths and a head-to-head (hh)/tail-to-tail (tt) magnetization configuration (see Fig. 1(a)).

Superparamagnetic beads (SPBs) interact with the MFL forming above the domain pattern, leading to their attraction towards locations of either hh or tt domain walls (DWs) in the underlying substrate. Superposing the MFL with a periodic sequence of trapezoidal magnetic field pulses applied in the  $x$ - and  $z$ -direction, a lateral stepwise motion of the SPBs is initialized. Each field pulse transforms the effective field acting on the SPBs, resulting in a periodically repeated magnetic force moving the SPBs sequentially from one DW position to the adjacent one (see Fig. 1(b)–(e)). We hypothesize that if the stripe domain width becomes too large, SPBs, depending on their magnetophoretic mobility, are not able to cross the distance to the adjacent DW in time, before a new field pulse is applied. Thus, the domain pattern and the resulting MFL are designed to allow for the controlled spatial separation of SPBs with differing  $U_m$  within a continuous experiment, where none of the external field parameters need to be adjusted. This concept, therefore, possesses the potential to enable a straightforward time-efficient operation, which goes beyond the frequency-based separation method established in literature, *e.g.* ref. 14 and 25, that typically focuses on highly symmetrical micromagnetic structures.

## 2 Experimental

### 2.1 Fabrication of magnetically patterned substrate

A magnetic parallel-stripe domain pattern with gradually changing stripe width (stripe length equal to substrate size of *ca.* 10 mm) and a periodic head-to-head (hh)/tail-to-tail (tt) magnetization configuration was imprinted into an exchange-biased (EB) thin film system *via* IBMP.<sup>31–33</sup> The thin film system consisted of a Cu(5 nm)/Ir<sub>17</sub>Mn<sub>83</sub>(30 nm)/Co<sub>70</sub>Fe<sub>30</sub>(10 nm)/Si(20 nm) layer stack, which was deposited onto a naturally oxidized Si(100) wafer piece (*ca.* 10 mm × 10 mm) by rf-sputtering at room temperature. Subsequently, the sample was field cooled to set the in-plane direction of the EB. For this, the sample was placed in a vacuum chamber (base pressure =  $5 \times 10^{-7}$  mbar) and annealed at 300 °C for 60 min in an in-plane magnetic field of 145 mT. In this state, the sample was ready for IBMP. Therefore, a homogeneous photoresist, with a sufficient thickness to prevent 10 keV He ions from penetrating the magnetic layers, was deposited on top of the thin film system *via* spin coating. The photoresist was structured to exhibit covered and uncovered areas of varying width and an equal length that corresponds to the size of the sample, using direct laser writing lithography. Starting with an uncovered stripe width of 1.2 μm, the adjacent covered stripe had a width of 1.5 μm, followed by another uncovered stripe of 2 μm. This alternation of covered and uncovered areas with gradually increasing widths was repeated with an increment of 0.5 μm until a stripe width of 5 μm was reached. For this width, the alternation of covered and uncovered areas was repeated eleven times. In the following, covered and uncovered areas were further widened with an increment of 0.5 μm until a width of 10 μm was finally reached.

These widest covered and uncovered resist areas were repeated seven times. Finally, the width of covered/uncovered areas was decreased back to the starting value of 1.2 μm, following the same incrementation parameters as for the width increase. This increase/decrease procedure is repeated periodically throughout the whole substrate area. Fig. S1 in the SI presents a local microscope image of the resist structure design. The long axis of the stripes was oriented perpendicular to the initial EB direction (set by the field cooling procedure). After resist structure fabrication, the sample was bombarded with a dose of  $1 \times 10^{15}$  cm<sup>-2</sup> He ions (kinetic energy of 10 keV) employing a home-built Penning ion source.<sup>34</sup> This ion dose suffices to create a stable remanent domain pattern, with no remagnetization induced by the weak field pulses employed in the transport experiment. For a periodic hh/tt magnetization of adjacent stripe domains, an in-plane homogeneous magnetic field (100 mT) was applied during ion bombardment, pointing antiparallel to the direction of the EB initializing field employed in the field cooling procedure. After bombardment, the photoresist was removed by washing the sample thoroughly with acetone. Finally, the sample surface was cleaned by rinsing it with acetone, isopropanol, and water.



After drying, a 500 nm thick poly(methyl methacrylate) (PMMA) spacing layer was deposited on top of the sample *via* spin coating.

## 2.2 Computation of magnetic stray field landscape

The simulation package MuMax3 (ref. 35) was used to compute the magnetization distribution  $\vec{m}(x, y)$  within a region of interest for the investigated stripe domain pattern with gradually increasing stripe width. Depending on whether stripe regions were bombarded/non-bombarded during the fabrication procedure, differing magnetic properties were assigned: an exchange stiffness constant of  $A_{\text{ex}} = 3 \times 10^{-11} \text{ J m}^{-1}$ ,<sup>36</sup> a saturation magnetization of  $M_s = 1.23 \times 10^6 \text{ A m}^{-1}$ ,<sup>37</sup> a uniaxial anisotropy constant of  $K = 4.5 \times 10^4 \text{ J m}^{-3}$ ,<sup>38</sup> for the non-bombarded stripes, and accordingly  $A_{\text{ex}} = 3 \times 10^{-11} \text{ J m}^{-1}$ ,  $M_s = 1.18 \times 10^6 \text{ A m}^{-1}$ ,  $K = 3.375 \times 10^4 \text{ J m}^{-3}$  for the bombarded stripes. The saturation magnetization and anisotropy constant are slightly reduced for the bombarded regions, as reported in previous publications.<sup>37,39</sup> For implementing the EB-related pinning of the respective domain magnetizations, additional biasing magnetic fields were defined for bombarded/non-bombarded stripes with opposing directions. Here, the magnetic flux densities were chosen to be 13 mT for the non-bombarded regions and 6.7 mT for the bombarded stripes according to experimentally determined values from hysteresis loop measurements. The region of interest was discretized into cubic mesh elements of  $5 \text{ nm} \times 5 \text{ nm} \times 10 \text{ nm}$ . The simulation software computed the relaxed magnetization state of the described system, giving a distribution of magnetic moments  $\vec{m}_i$  for each mesh element  $i$ . It was subsequently used for obtaining magnetic stray field components  $\vec{H}_x(\vec{r})$  and  $\vec{H}_z(\vec{r})$  (see Fig. 1(f and g)) *via* the following dipole approximation:<sup>40</sup>

$$\vec{H}(\vec{r}) = \frac{1}{4\pi} \cdot \sum_i \frac{3\vec{R}(\vec{R} \cdot \vec{m}_i)}{|\vec{R}|^5} - \frac{\vec{m}_i}{|\vec{R}|^3}. \quad (2)$$

$\vec{R} = \vec{r} - \vec{r}_i$  represents the distance vector between position  $\vec{r}$  and dipole position (mesh element position)  $\vec{r}_i$ .

## 2.3 Transport of superparamagnetic beads

For inducing the directed motion of SPBs, 20  $\mu\text{L}$  of a diluted aqueous dispersion of SPBs (Dynabeads M-270 Carboxylic Acid/Dynabeads MyOne) was pipetted on top of the magnetically patterned substrate. The fluid containing the SPBs was confined by a microfluidic chamber that was adhered to the substrate surface. The chamber was produced by cutting a square of approximately  $8 \text{ mm} \times 8 \text{ mm}$  out of a  $10 \text{ mm} \times 10 \text{ mm}$  sized Parafilm sheet. The chamber was sealed by a square-shaped glass coverslip and the substrate with the SPBs on top was placed in the center of a Helmholtz coil arrangement. Within this arrangement, orthogonally placed Helmholtz coils allowed for the application of homogeneous trapezoidal magnetic field pulses perpendicular and parallel to the transport substrate plane, *i.e.*, the  $z$ - and  $x$ -direction. The substrate itself was aligned

with the substrate plane normal pointing parallel to the  $z$ -direction and the in-plane magnetization direction pointing parallel to the  $x$ -direction (see Fig. 1). Each magnetic field pulse consisted of a linear rising time, a plateau time, and a linear drop time. The rising and drop times were determined by the pulse magnitude  $H_{\text{max}}$  as well as the alteration rate of the external magnetic field being  $3.2 \times 10^6 \text{ A m}^{-1} \text{ s}^{-1}$ . The pulse magnitudes were chosen to be  $\mu_0 H_{\text{max},x} = 1 \text{ mT}$  for the  $x$ -direction field and  $\mu_0 H_{\text{max},z} = 1 \text{ mT}$  or  $2 \text{ mT}$  for the  $z$ -direction field. For the initialization of directed SPB motion, a temporal phase shift of  $\pi/2$  between pulse sequences in the  $z$ - and  $x$ -direction and a periodic change of pulse orientation between  $H_{\text{max}}$  and  $-H_{\text{max}}$  was implemented (see Fig. 1(a)). For observing and recording the SPB motion, the sample was approached with an optical bright-field microscope in reflection mode. SPB motion was recorded with an attached high speed camera: both a Mikrotron EoSens CoaXPress CXP-6 camera (maximum resolution of  $4096 \text{ px} \times 3072 \text{ px}$ ) at a framerate of either 25 frames per second (fps) or 10 fps and an Optronis CR450x2 camera (maximum resolution of  $800 \text{ px} \times 600 \text{ px}$ ) at a framerate of 1000 fps were employed for SPB transport characterization.

## 3 Results

### 3.1 Qualitative investigation

SPBs with a diameter of  $2.8 \mu\text{m}$  were placed on top of an EB thin film substrate magnetically patterned by IBMP. The pattern consists of parallel stripe domains with gradually increasing/decreasing stripe width and a periodic in-plane hh/ht magnetization configuration (see Fig. 1(a)). Fig. 1(f and g) presents the magnetic stray field distributions for  $H_x$  and  $H_z$  emerging above the substrate at a distance of  $z = 2500 \text{ nm}$  away from the magnetic thin films. Maxima and minima of  $H_z$  are located above DW positions, while, conversely, maxima and minima of  $H_x$  can be found in the center between two DWs. An aqueous dispersion of the SPBs was pipetted onto the magnetically patterned substrate (covered by a 500 nm thick PMMA layer) and a sequence of trapezoidal magnetic field pulses in  $z$ - and  $x$ -direction (see Fig. 1(a)) was applied after letting the SPBs sediment towards the substrate surface. Fig. 2(a) presents a microscope image taken before applying the external fields ( $t = 0.0 \text{ s}$ ). For better recognition of SPBs, the background of the image, containing inhomogeneous illumination and substrate defects, was subtracted and a denoising algorithm was applied.

SPBs are statistically distributed across the field of view in this initial state. The approximated positions of stripe DWs in the underlying substrate are indicated by dashed black lines. For the lateral  $x$ -coordinate, SPBs are mostly located directly above or very close to a DW, owing to the attraction toward maximum stray field strength. Upon initiating an external magnetic field pulse sequence with a period of  $T = 0.4 \text{ s}$  and pulse amplitudes of  $\mu_0 H_{z,\text{ext}} = \mu_0 H_{x,\text{ext}} = 1 \text{ mT}$  in  $z$ - and  $x$ -direction, respectively, SPBs performed a stepwise motion in positive  $x$ -direction, towards increasing stripe



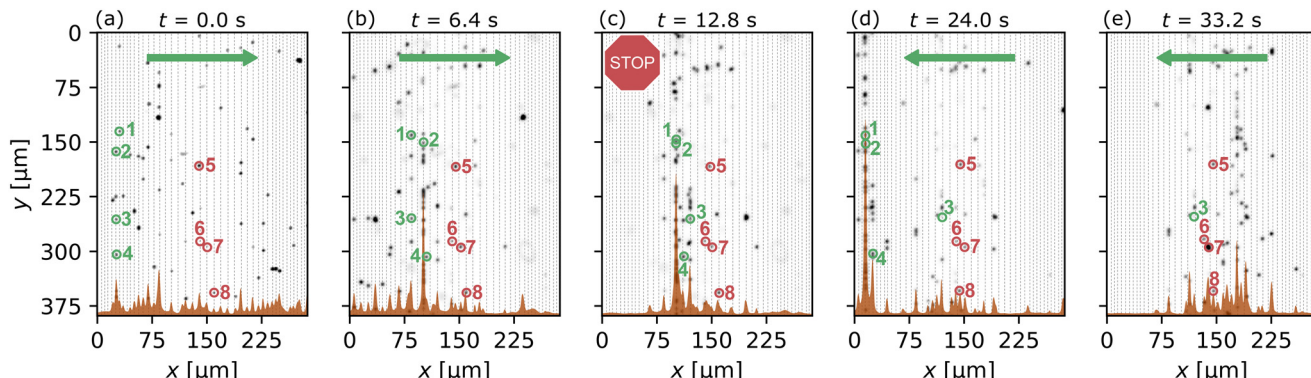


**Fig. 2** Optical analysis for the motion behavior of SPBs dispersed in water on top of a magnetic stripe domain pattern with gradually varied stripe width. Shown are single optical microscope images (a)–(e) obtained at different recording times  $t$  of a video recording taken with a frame rate of 25 fps. For the recorded experiment, a periodic sequence of trapezoidal magnetic field pulses with  $T/4 = 0.1$  s and  $\mu_0 H_{\max,x} = \mu_0 H_{\max,z} = 1$  mT was applied. The stripe domain pattern within the underlying substrate is indicated in each displayed frame by black dashed lines. Throughout the frames, eight exemplary SPBs are highlighted by either green circles (initially mobile) or red circles (initially immobile). Numbers are assigned to these SPBs so that their change in position can be traced. For frames (a) and (b), SPBs (black spots) are transported from left to right across the substrate (see green arrows), leading eventually to immobilization at a lateral  $x$ -position of ca. 100  $\mu\text{m}$ , prominently visible in (c). Here, the external field sequence was stopped and paused for 8 s, resulting in a halted SPB motion. Upon re-initialization of the external field sequence with inverted phase relation between field pulses in  $z$ - and  $x$ -direction, SPBs are transported into the opposite direction, emphasized in (d) and (e) by the green arrows. Frame (e) highlights the immobilization of SPBs this time around ca. 200  $\mu\text{m}$   $x$ -position. Lateral particle density profiles, averaged along the  $y$ -dimension, are included as brown-filled curves in each frame.

domain width, *i.e.*, increasing DW separation distances. Reaching a certain DW separation distance, SPBs began to perform oscillating movements along the lateral  $x$ -dimension, effectively losing their transportability and being, therefore, classified as immobile. SPBs located at the substrate area of maximum DW separation directly after sedimentation showed this oscillatory motion from the start of the external field sequence. At  $t = 6.4$  s, the gradual SPB immobilization was observable by an increasing accumulation of SPBs at a lateral position of  $x \approx 100$   $\mu\text{m}$  (Fig. 2(b)) though a few SPBs were immobilized even earlier, starting from around 60  $\mu\text{m}$   $x$ -position. Here, SPBs are prominently caught between 9.0  $\mu\text{m}$  and 9.5  $\mu\text{m}$  wide stripe domains. After  $t = 12.8$  s, all SPBs moving from left to right are immobilized, leading to a maximum accumulation of SPBs at the largest DW separations (Fig. 2(c)). The external fields were stopped at this moment. Probing whether SPBs can regain their transportability, a pulse sequence with inverted phase relation between fields in  $z$ - and  $x$ -direction was applied after a pause, initiating SPB transport in the opposite direction. As a consequence, formerly immobilized SPBs at  $\approx 100$   $\mu\text{m}$   $x$ -position could be transported from right to left, as can be seen for  $t = 24.0$  s in Fig. 2(d). At the end of the experiment, at  $t = 33.2$  s, SPBs were accumulated at an  $x$ -position of  $\approx 200$   $\mu\text{m}$ . They represent SPBs that were previously immobilized at larger DW separation distances not seen in the field of view, owing to the periodic repetition of increasing/decreasing stripe domain width. After inverting the phase relation for the external field sequence, they were transported back into the field of view and finally immobilized again at larger DW separation distances.

Starting from this general observation, exemplary single SPBs (highlighted in Fig. 2(a)–(e) by green and red circles)

were followed more closely to analyze their immobilization efficiency. Four SPBs (1–4) were located at a stripe domain width of 5  $\mu\text{m}$  at the beginning of the experiment, *i.e.*, after particle sedimentation, while four other SPBs (5–8) were positioned at a stripe domain width of 10  $\mu\text{m}$ . The latter fraction of SPBs proved to be immobile (oscillating motion) throughout the displayed frames (a)–(e) in Fig. 2, resulting in no significant change in their lateral  $x$ -position. Particles 1–4, however, were transported during the first sequence of externally applied field pulses towards wider stripe domains, eventually being immobilized once they could not reach the adjacent DW in time (see Fig. 2(c)). Upon inducing SPB transport in the opposite direction (Fig. 2(d)), only particle 3 stays immobilized, most probably because it was pushed by other incoming particles to a region of maximum stripe domain width. The other SPBs regained their mobility since the reversed transport direction allowed them to perform shorter jumps due to a decreased DW separation distance. Overall, 37 SPBs were located at the region of maximum stripe domain width (10  $\mu\text{m}$ ) before starting the experiment, rising to 86 particles after finishing the first external pulse sequence due to the gradual immobilization of incoming particles. When applying the second pulse sequence with inverted transport direction, 74 SPBs stayed in this region after the mobile fraction of particles had left. Once this sequence has finished as well, the number rose again to 104 SPBs because particles coming from the opposite side are gradually immobilized in this instance. As a consequence, a reduction of the mobile SPBs was observed when applying consecutive external pulse sequences with inverted phase relation (leading to different transport directions).

From the initial experiment, first evidence for the fractionation capability of the investigated domain pattern

design is collected. For studying the SPB motion behavior in more detail, continuous tracking of SPB rows was realized by looking at the time dependence of lateral intensity profiles, as a measure for SPB density, within each recorded image frame of the transport experiment. These profiles represent the image pixel grey scale values along the  $x$ -dimension and were averaged for each image along the  $y$ -direction to get the mean position information for each SPB row. Examples of the intensity profiles are documented as brown-filled curves in each image of Fig. 2(a)–(e). Peaks within the profiles mark the momentary lateral positions of single SPB rows. Plotting the lateral intensity profiles of all images that were recorded during the experiment as a function of time creates a 2D false-color image that enables the tracing of each SPB row position throughout the experiment. Using this evaluation method, the qualitative SPB motion behavior can be visualized more intuitively and the influence of changing experimental parameters can be detected at first glance.

For instance, Fig. 3(a) shows the map of lateral intensity profiles in dependence on experimental time for the initially described transport experiment of Fig. 2. Continuous lines of high intensity (low grey scale value) mark the trajectories of single SPB rows, whereby the absolute grey scale value correlates antiproportionally with the number of particles present in a specific row.

Initially, SPBs are transported from left to right through the field of view, leading to diagonal intensity lines, except

for the substrate region, where SPBs perform oscillating movements from the beginning. This is the case for a region between  $\approx 60$   $\mu\text{m}$  and  $\approx 200$   $\mu\text{m}$  lateral  $x$ -position, which is therefore highlighted in Fig. 3(a) by two dashed white lines. Over time, SPBs are either approaching this region from the left or leaving this region to the right. For most of the approaching SPBs, it could be observed that they eventually transition to oscillating movement, most prominently before the stripe domain width increases to 9.5  $\mu\text{m}$ . This is mirrored in the intensity map of Fig. 3(a) by a zig-zagging line at  $\approx 100$   $\mu\text{m}$   $x$ -position, with an increase of intensity (decrease of grey scale value) observable for this line over time. Thus, an increasing number of approaching SPBs was immobilized at this position, accounting for the rising SPB density. Some SPBs transition to oscillating motion at larger stripe domain widths or even continue their directed motion, *i.e.*, they are transported beyond the immobilization region. These SPBs acquire larger motion velocities, most likely due to a larger magnetophoretic mobility (see eqn (1)). Hence, they are enabled even for the largest stripe domain width (10  $\mu\text{m}$ ) to traverse the distance between two neighboring DWs in phase with the transformation of the MFL by the external fields. This physical mechanism will be analyzed in more detail in the Discussion section. Stopping the external field sequence at  $t \approx 13$  s (marked by the lower horizontal white line in Fig. 3(a)), the SPBs rest at their immobilized position, indicated by straight lines in the intensity map. After  $t \approx 21$  s

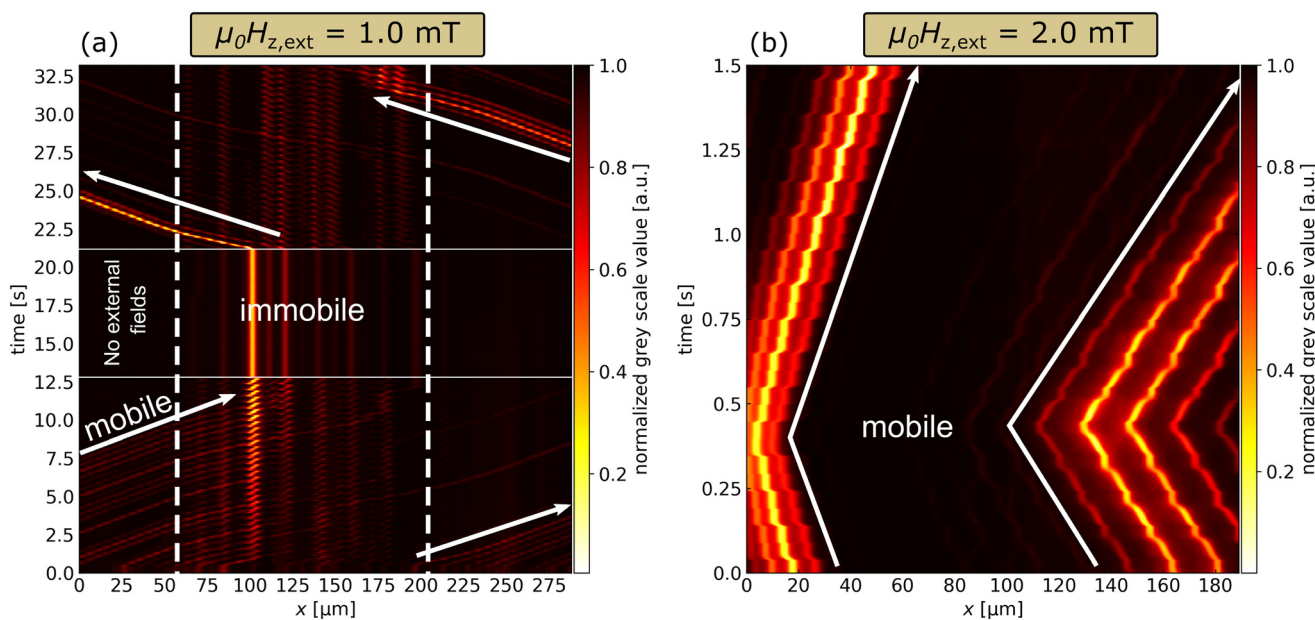


**Fig. 3** Motion behavior of SPBs dispersed in water on top of a magnetically patterned substrate with increasing stripe domain width for two different external magnetic field amplitudes in  $z$ -direction. A qualitative impression of the SPB transport is given by presenting averaged lateral intensity profiles of each recorded image frame as a function of recording time. The color scale indicates the image intensity; high intensity represents the background and low intensity the presence of SPB rows. For weak external magnetic field pulses of  $\mu_0 H_{z,\text{ext}} = \mu_0 H_{x,\text{ext}} = 1.0$  mT magnitude (a), fractions of mobile and immobile SPBs were distinguishable in dependence on the substrate position. The immobilization of SPBs occurred at a substrate area between  $\approx 60$   $\mu\text{m}$  and  $\approx 200$   $\mu\text{m}$  lateral  $x$ -position (marked by dashed white lines), coinciding with the substrate region of largest stripe domain width. Mobile SPBs were initially transported from left to right until immobilization. After a pause, the external field sequence was modified so that SPB transport from right to left was initiated. Most of the previously mobile SPBs regained their mobility by this. Stronger field pulses of  $\mu_0 H_{z,\text{ext}} = 2$  mT magnitude (b) lead to mobilization of SPBs even for the region of largest stripe domain width.

(marked by the upper horizontal white line in Fig. 3(a)), an adjusted field sequence leads to transport of immobilized SPBs towards the left edge of the field of view. It is most prominently visible that almost all SPBs immobilized at  $x \approx 100 \mu\text{m}$  regained their transportability and could be relocated. SPBs that stay in the immobilized region are mostly those that were already located there from the start of the experiment, *i.e.*, after sedimentation. They supposedly don't possess sufficient magnetophoretic mobility to traverse the respective DW separation distance. Mobile SPBs that approached the region of largest stripe domain width from the right yielded similar observations: they either transitioned to oscillatory motion at a certain DW separation distance or, in a few rare cases, maintained their directed motion. A large group of SPBs entering the field of view at  $t \approx 27.5 \text{ s}$  was prominently immobilized at  $x \approx 175 \mu\text{m}$ . These SPB rows arrived in close succession since they were immobilized according to their respective magnetophoretic mobility at large stripe domain widths outside of the chosen field of view. For studying the influence of the external field strength on the SPBs' transportability, a similar experiment was conducted with a magnitude of  $\mu_0 H_{z,\text{ext}} = 2 \text{ mT}$  for the field pulses in  $z$ -direction, while the pulses in  $x$ -direction were kept at  $\mu_0 H_{x,\text{ext}} = 1 \text{ mT}$  magnitude. The result for a 1.5 s long segment of this experiment is displayed in Fig. 3(b). Two fractions of SPBs are visible, one at the right edge and one on the left edge of the field of view. The right fraction is located at larger DW separation distances than the left fraction. Remarkably, even the fraction at the largest DW separation distances shows continuous transportability in both directions, which was not true for the lower external field strength. For this particular experiment, even a decreased period  $T = 0.2 \text{ s}$  still allowed for continuous SPB transport throughout the whole substrate area, owing to the increased external field strength. The transportability of the right fraction must, therefore, be connected to a larger magnetic force acting on the SPBs with the increased magnitude of  $H_{z,\text{ext}}$ . With a larger driving force, SPBs gain in their motion velocity and are consequently enabled to follow the transformation of the MFL in phase. To quantify this increase in motion velocity, single SPBs were measured to achieve an average maximum velocity (acquired during a transport step) of  $150(20) \mu\text{m s}^{-1}$  for 1 mT  $H_z$  pulse magnitude, while for 2 mT the velocity sprung up to  $220(20) \mu\text{m s}^{-1}$ . The results suggest that the external field strength is a regulator for controlling SPB mobility towards specific applications.

### 3.2 Quantitative analysis of step velocity

A deeper analysis uncovered an additional dependency of the SPB steady-state velocity (the velocity acquired by an SPB after its acceleration phase) on the current lateral position above the substrate. More specifically, it depends on the distance traveled by the SPB during one motion cycle, *i.e.*, the DW separation distance. The analysis was carried out by initiating

SPB movement over the whole substrate area, thus inducing transport steps for all DW separation distances.

The following parameters for the external magnetic field pulse sequence were, therefore, chosen in order to avoid immobilization of the SPBs:  $\mu_0 H_{z,\text{ext}} = 1 \text{ mT}$ ,  $\mu_0 H_{x,\text{ext}} = 1 \text{ mT}$  and  $T = 0.8 \text{ s}$ . The increase in  $T$  gave the SPBs sufficient time to follow the transformation of the MFL in phase and thereby maintain continuous transportability. Microscope images of the experiment were recorded for 8 s at a frame rate of 1000 fps and averaged lateral particle density profiles were determined for every image. The evolution of these profiles over time is shown in Fig. 4(a), indicating transport of SPB rows from left to right through the field of view. From a qualitative point of view, small transport steps within the SPB row trajectories can be observed for lower  $x$ -positions, while with larger  $x$ -position the distance per step is increasing. The trajectories of 19 SPB rows are traceable in total for this intensity profile map. Two trajectories were handpicked to serve as exemplary trajectories for the following description and visualization of steady-state velocity determination and its dependency on the SPB transport step distance. The starting and end positions of these trajectories are marked with purple and green arrows in Fig. 4(a), respectively. They were chosen because a wide range of DW separation distances from  $2 \mu\text{m}$  to  $10 \mu\text{m}$ , *i.e.*, a wide range of SPB transport step distances are covered herein. It needs to be emphasized at this point that no single particle analysis was taken into account, for the reason that single particle tracking was not feasible for the experimentally obtained SPB densities. As we were interested in the general development of SPB steady-state velocity with increasing stripe domain width, the tracking of SPB rows *via* lateral intensity profiles sufficed.

The SPB row motion consists of two distinguishable phases: a transport phase towards the adjacent DW that is induced with the application of magnetic field pulses in  $z$  and  $x$ -direction, as well as a resting phase where the motion of the SPBs is completed and the application of the next field pulse is awaited. Both phases can be observed more closely by showing 400 ms long snippets of the exemplary trajectories in Fig. 4(b)–(d). The position of each snippet within the overall SPB row trajectory is marked by white shaded areas in Fig. 4(a). Note that the visualization is now reversed, plotting the  $x$ -position data for intensity peaks in the map of Fig. 4(a) as a function of time  $t$ . Each snippet contains a larger transport step, which results from applying a field pulse in the  $z$ -direction, and a smaller transport step, which is the consequence of a field pulse in the  $x$ -direction (comparable to previous studies for hh/tt stripe domains of equal widths<sup>15,23</sup>). The resting phase of SPBs is signified by plateaus in the  $x(t)$  data. The larger transport step was used to determine the steady-state velocity of SPBs (averaged for all SPBs residing in the same row) during one motion event and the accompanying transport step distance. For doing so, each larger step was placed into a  $x(t)$  slice of 200 ms as indicated by the red shaded areas in Fig. 4(b)–(d). A Gaussian error function was used as an approximation for the  $x(t)$  data



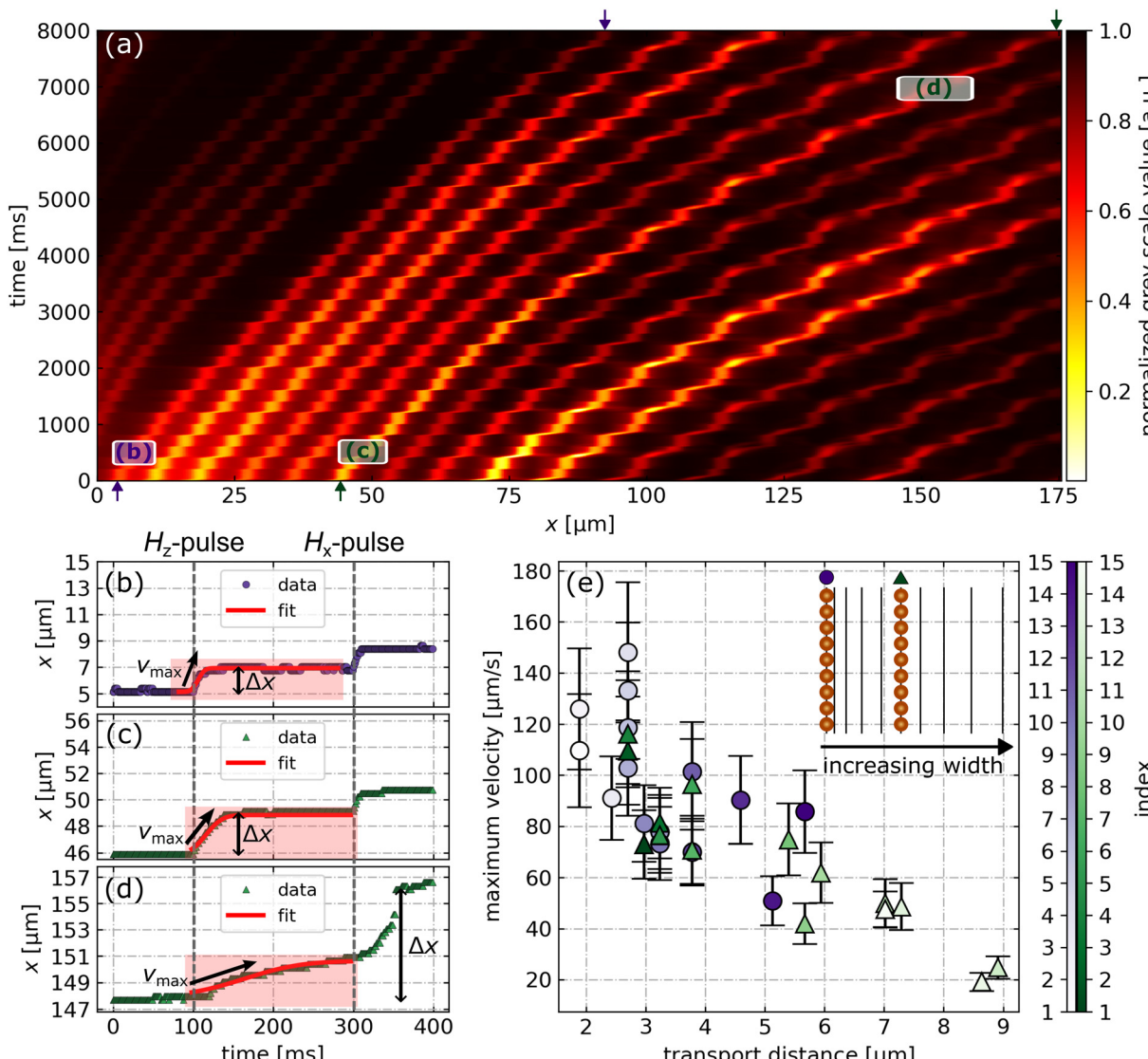


**Fig. 4** Quantitative analysis of SPB motion dynamics in water above a magnetically patterned substrate with increasing stripe domain width. Starting from the evolution of averaged lateral intensity profiles acquired from each recorded image frame during the experiment (a), three SPB row trajectory snippets highlighted with white-framed rectangles were picked as examples for the identification of maximum particle velocity in (b)–(d). Here, grey dashed lines indicate the times when an external magnetic field pulse was applied, i.e., the sign of the external field magnitude was reversed for the respective direction. The period of the external magnetic field pulse sequence was chosen to be  $T = 0.8$  s with pulse magnitudes of  $\mu_0 H_{z,\text{ext}} = \mu_0 H_{x,\text{ext}} = 1$  mT to initiate SPB transport from left to right throughout all domain widths present in the underlying substrate (no immobilization). Maximum SPB row motion velocities, as a measure for their averaged mobility, were determined for the transport step initiated after changing the sign of the external field in  $z$ -direction. The red-marked areas for the exemplary trajectory data  $x(t)$  in (b)–(d) were considered for the velocity calculation by fitting a Gaussian error function to the marked data (shown as red solid lines) and subsequently obtaining the velocity as the maximum of the fit's time derivative. Each velocity is assigned a transport step distance  $\Delta x$ , which corresponds to the difference between two consecutive plateaus in the trajectory data (see further explanation in the text). Plotting the obtained velocities as a function of the respective transport distance for the two SPB row trajectories that contain the exemplary steps of (b)–(d), a decreasing tendency for the velocity with larger transport steps (larger domain width) is observable (e).

during the transport step and therefore fitted to each slice. A distribution of velocities over time  $v(t)$  was retrieved by computing the derivative of the obtained fit function. The maximum  $v_{\text{max}}$  of the distribution was chosen as a measure for the steady-state velocity of the respective SPB row. The steady-state velocity is governed by an equilibrium of magnetic and friction force, theoretically leading to trajectory data of constant slope. As there are no regions of constant

slope within the Gaussian error fit function, the obtained maximum velocity can only be an approximation for the real steady-state velocity. This is taken into consideration for the error of the velocity, which was determined by averaging over all values present above the full width at half maximum (FWHM) of the obtained distribution and calculating the difference of this averaged velocity to  $v_{\text{max}}$  (see Discussion section).



Qualitative changes in  $v_{\max}$  can be made out when comparing the trajectory snippets of Fig. 4(b)–(d), where each snippet represents a different transport step distance. The transport step distance was characterized as the difference  $\Delta x$  between two adjacent  $x(t)$  plateaus. After initiation of the larger transport step at  $t = 100$  ms, the next plateau is reached after a few milliseconds for the exemplary data shown in Fig. 4(b) and (c), indicating a comparably fast SPB row motion. The transport step distance  $\Delta x$  is increasing from (b) to (c), the steady-state velocity  $v_{\max}$ , however, appears to decrease. This trend continues for the exemplary data of Fig. 4(d) that represents SPB motion above the substrate area with maximum DW separation distance. Remarkably, the SPB row motion is induced with a delay when compared to the previous transport steps, starting around 110 ms instead of 100 ms (a physical explanation is provided in the Discussion section). The ensuing motion is visibly slower and also does not come to a full stop before  $t = 300$  ms, where an external field pulse in the  $x$ -direction is applied. This induces the smaller transport step, which can be identified more clearly in Fig. 4(b) and (c). In these instances, the SPB rows have already come to rest above the adjacent DW position before the initiation of the smaller step. For the step presented in Fig. 4(d), the SPB row has not yet reached the position of the adjacent DW. Determining  $\Delta x$  at this time would, therefore, not reflect the corresponding separation distance of neighboring DWs in the underlying substrate for this particular transport step. The additional transformation of the MFL by an applied pulse in the  $x$ -direction triggers another acceleration phase for the SPB row. The SPBs finally come to rest after around  $t = 350$  ms, marking the approximate location of the adjacent DW and therefore making it possible to quantify  $\Delta x$  for larger DW separation distances. For the sake of comparability,  $v_{\max}$  is determined in this case only for the first induced motion phase, as indicated in Fig. 4(d). Evaluating  $v_{\max}$  for every larger transport step within the two selected SPB row trajectories in dependence on the transport step distance  $\Delta x$  yields the result shown in Fig. 4(e).

Data points measured for the first SPB row (starting at the substrate area of lowest DW separation distance) are represented by purple circles and data points measured for the second SPB row (starting at the region of larger DW separation distances) by green triangles. The color scale for the data points indicates the transport step index, *i.e.*, the occurrence of the transport step within the analyzed trajectory. The lower the index, the earlier the transport step was observed (typically at a lower DW separation distance). The correlation between  $v_{\max}$  and  $\Delta x$  reflects the qualitative trend: with increasing transport distance of the SPBs (DW separation distance), the steady-state velocity is lowered, from over  $140 \mu\text{m s}^{-1}$  for the lowest transport distances down to  $20 \mu\text{m s}^{-1}$  for the largest steps. It has to be noted that not all transport steps within the two trajectories could be evaluated for  $v_{\max}$  due to insufficient fit quality. Therefore, some data

points are missing, most prominently for the largest transport distances, which, however, does not lessen the clarity of the observed trend. It becomes even more evident when looking at the steady-state velocities obtained from the analysis of all visible SPB row trajectories shown in Fig. S2 in the SI. In terms of SPB fractionation efficiency, the beads' mobility is significantly decreased for larger domain widths in the underlying substrate due to the lowered motion velocity, leading to the observed oscillatory behavior for smaller periods of the external field sequence. A physical explanation for this correlation will be approached in the Discussion section.

### 3.3 Fractionation of differently-sized beads

According to eqn (1), the magnetophoretic mobility of an MP transported by magnetic field gradients within a liquid environment is determined by its hydrodynamic radius and magnetic moment, given that the properties of the liquid stay constant. Therefore, we probed the fractionation of MP species with significantly different magnetophoretic mobilities by observing a mixture of differently-sized SPBs in the same experiment. Hence, an aqueous mixture of Dynabeads MyOne ( $d = 1 \mu\text{m}$ ) and Dynabeads M-270 ( $d = 2.8 \mu\text{m}$ ) was prepared and placed on top of the substrate with varying magnetic stripe domain width covered by a 500 nm thick PMMA layer.

To initiate the fractionation experiment, the majority of all present SPBs were transported to the substrate area of smallest stripe domain width, choosing the appropriate external magnetic field sequence. The achieved distribution of SPBs before the start of the experiment ( $t = 0$  s) is shown in Fig. 5(a). An averaged lateral intensity profile (brown-filled curve) is included to highlight the position of SPB rows and the number of SPBs per row. For this starting condition, SPBs of all sizes are assembled in rows on top of the DWs in the underlying substrate with an overall random distribution of  $d = 1 \mu\text{m}$ - and  $d = 2.8 \mu\text{m}$ -sized beads within each row. A sequence of external magnetic field pulses ( $\mu_0 H_{z,\text{ext}} = 2 \text{ mT}$ ,  $\mu_0 H_{x,\text{ext}} = 1 \text{ mT}$ ,  $T = 0.08 \text{ s}$ ) was applied, with the phase relation between pulses in  $z$ - and  $x$ -direction defined so that SPBs are moving from the left to the right through the field of view. Due to the relatively short period of the applied sequence, SPBs are traversing the imaged substrate area in under one second, emphasized by the snapshot taken at  $t = 0.56 \text{ s}$  in Fig. 5(b). At this point, the differently-sized SPBs are moving simultaneously and their spatial distribution is, therefore, still statistically defined. This changes after a few seconds: all SPBs are immobilized (oscillatory motion around a DW position) with an observable separation of the two SPB species at different substrate areas. The image shown in Fig. 5(c) marks the end of the experiment at  $t = 3.84 \text{ s}$  and highlights the final spatial distribution of the SPBs. While  $1 \mu\text{m}$ -sized beads are most prominently located at  $x$ -positions between  $40 \mu\text{m}$  and  $100 \mu\text{m}$ ,  $2.8 \mu\text{m}$ -sized beads reached further across the substrate and were immobilized at



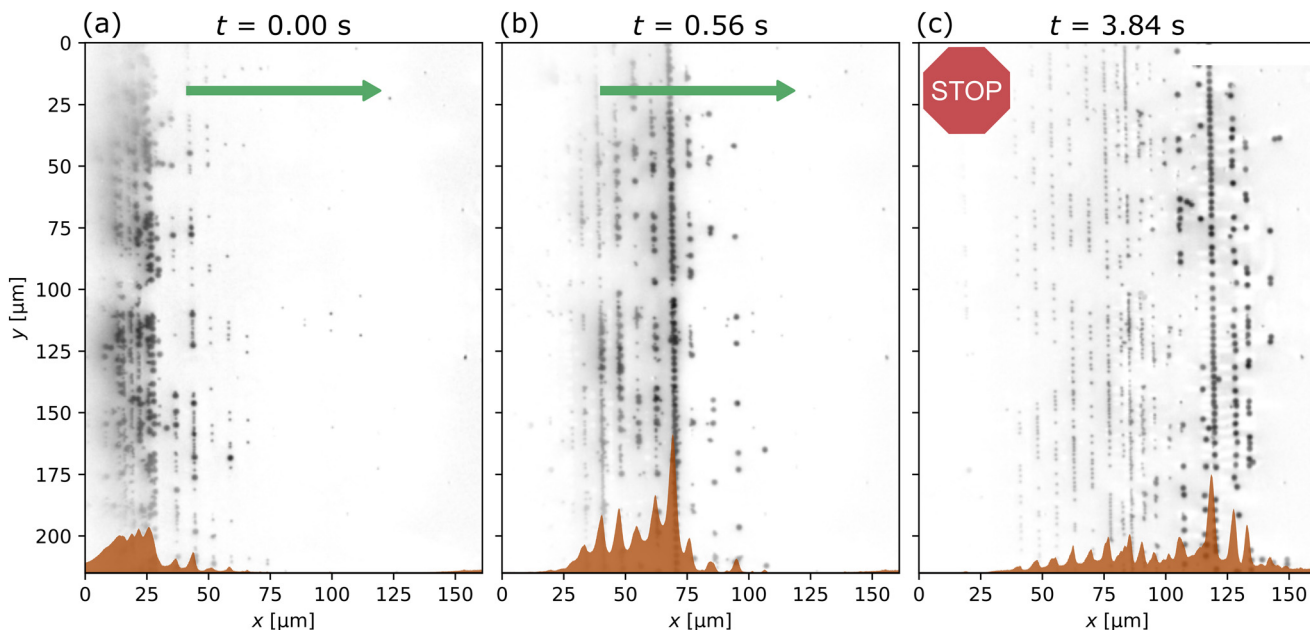


**Fig. 5** Fractionation of differently-sized SPB populations on top of a magnetically stripe domain patterned substrate with increasing stripe width. (a) All SPBs are assembled on the left edge of the microscope's field of view, resembling minimal stripe domain width in the underlying substrate. (b) Upon application of an external magnetic field pulse sequence of constant frequency, all SPBs are transported to the right side of the field of view. (c) After a short time, the SPBs are immobilized (oscillatory motion) at specific locations. Statistically, smaller SPBs ( $d = 1 \mu\text{m}$ ) are immobilized earlier (at lower lateral x-position) than larger SPBs ( $d = 2.8 \mu\text{m}$ ). The two SPB populations were spatially separated into distinguishable fractions. Averaged intensity profiles (brown-filled curves) indicate the lateral extent of each fraction above the substrate surface.

x-positions between  $100 \mu\text{m}$  and  $150 \mu\text{m}$ . Overall, Dynabeads M-270 proved to have higher magnetophoretic mobility, as known from literature,<sup>41</sup> therefore being enabled to traverse larger DW separation distances than Dynabeads MyOne. Analogous to the previous observations for nominal equally sized SPBs, all beads of one species are not immobilized above one specific DW but are rather spread within an immobilizing region. Judging from the peak heights within the averaged lateral intensity profile shown in Fig. 5(c), which correlate with the number of SPBs present within one specific row, the majority of Dynabeads MyOne was immobilized at  $90 \mu\text{m}$  x-position and the majority of Dynabeads M-270 at  $120 \mu\text{m}$ . Supposedly, the reason for the observed broad distribution of SPBs lies within a statistical fluctuation of bead characteristics around the nominal value. Typically, commercially available batches of SPBs show some degree of polydispersity. In addition, some areas of the substrate consist of a repetition of  $5 \mu\text{m}$  and  $10 \mu\text{m}$  wide stripe domains. Here, minor variations in the local effective magnetic field and/or substrate surface properties might lead to SPB immobilization above different DWs. On average, however, the conducted proof-of-principle experiment emphasizes the capability of our MFL (domain pattern) design to create spatially separated fractions of MP species with significantly differing magnetophoretic mobilities. The fractions can be collected for further analysis by transporting them simultaneously, while still being separated, *via* magnetic field pulses with increased  $H_z$  magnitude (see results of Fig. 3(b)).

## 4 Discussion

The observed immobilization of SPBs for larger DW separation distances in the underlying magnetically patterned substrate can be traced back to two physical mechanisms. On the one hand, SPBs must traverse larger distances when a transport step is induced, effectively increasing the time  $t_{\text{step}}$  required for reaching the adjacent DW position when assuming a constant average velocity. If  $t_{\text{step}}$  is larger than a certain critical length of time  $t_{\text{crit}}$ , SPBs are more likely to slip back to their original position before the initialization of the next transport step, therefore, entering the so-called “phase-slipping” transport mode.<sup>25</sup> Both the literature and our study highlight that the period  $T$  of the external field sequence has a large impact on  $t_{\text{crit}}$ . In this work, we demonstrated that  $t_{\text{step}}$  can be deliberately adjusted by the separation distance of artificial DWs imprinted into an in-plane EB thin film system. As a result, the transition from directed SPB transport (“phase-locked” regime) to oscillating motion (“phase-slipping” regime) is a function of SPB position at constant  $T$ , *i.e.*, constant  $t_{\text{crit}}$ . On the other hand, the motion velocity of same-sized SPBs is not independent of the DW separation distance, as the quantitative investigation shown in Fig. 4 and S2 in the SI has demonstrated. Larger DW separation distances lead to lower maximum SPB velocities after the application of an external z-field pulse. This further contributes to an increased  $t_{\text{step}}$  and a higher probability for an SPB to switch to the “phase-slipping” regime. The observed trend itself is very



likely to originate either from a decreasing accelerating magnetic force or an increasing decelerating friction force. For assessing the magnetic force, the simulated static MFL on top of the substrate displayed in Fig. 1(f and g) will be considered. Starting at a domain width of 1  $\mu\text{m}$  and increasing the width gradually until 5  $\mu\text{m}$ , the results suggest an increasing stray field strength on top of the respective DWs. As an SPB's magnetic moment is proportional to the applied magnetic field strength, this would mean an increasing magnetic force with larger domain width, which seems to contradict the experimental observation. It does, however, provide a possible explanation for the delay in motion initialization observed for larger stripe domain widths (see Fig. 4(d)). With increasing magnetic attraction towards the underlying polymer surface, SPBs might get close enough for attractive van der Waals interactions to become more influential. In this case, the observed delay could be caused by an initial adherence of the SPBs to the polymer surface, eventually overcome by the magnetic force pushing the particles to the next DW location. What has not been considered at this point is the magnetic field gradient, determining the acting magnetic force together with the SPBs' magnetic moments. Confining the stray fields in a smaller volume (smaller DW separation distance) may lead to an increased field gradient and, in turn, an increasing magnetic force. This tendency could, however, be balanced out by the lower field strength for the smallest domain widths.

Finally, we may consider different hydrodynamic drag situations in dependence on the respective DW separation distance. For the smallest stripe domain width, where the stray field strength is the lowest, SPBs are expected to exhibit an increased separation distance from the underlying substrate surface due to lessened magnetic attraction. The friction force for a spherical particle moving close to a flat surface inside a fluid is, among others, a function of a  $z$ -position-dependent friction coefficient.<sup>42</sup> The correlation is hereby anti-proportional: with increasing distance  $z$  from the surface, the friction coefficient is decreased. The resulting reduced drag may partially explain the observed larger SPB motion velocities for the smallest transport step distances.

It was generally observed that for the chosen domain pattern design and a period  $T = 0.4$  s for the sequence of 1 mT strong magnetic field pulses, most of 2.8  $\mu\text{m}$ -sized SPBs were immobilized at a DW position between 9  $\mu\text{m}$  and 9.5  $\mu\text{m}$  wide stripe domains. As visible from Fig. 2(c) and 3(a), this is not true for all initially transported SPBs; some get immobilized at larger or lower DW separation distances, and a few even don't get immobilized at all. This reflects the spread of magnetophoretic mobility within a single badge of nominally equal-sized particles, as can also be deduced from the SPB fractionation experiment of Fig. 5. Grob *et al.* point out that judging from their experiments conducted to determine the magnetic susceptibility of commercially-available SPBs *via* measuring their magnetophoretic mobility in a constant gradient field, this spread may only be due to

variations in the SPBs' magnetic content.<sup>41</sup> The size variation of <3%, as claimed by the manufacturer, was confirmed by Grob *et al.* with structural measurements,<sup>41</sup> rendering its influence on the spread of magnetophoretic mobility as insignificantly small. The distribution of magnetic susceptibility for the utilized SPBs (Dynabeads M-270) is, for now, not known to us. Acquiring exact knowledge on the magnetic stray field distribution above the magnetically patterned substrate with future measurements, one could determine the distribution of SPBs' magnetic susceptibility within one particle badge by precisely calculating the magnetic force acting on the SPBs.

Our MFL design is demonstrated to enable sorting of SPBs by their mobility, so that subsequent bio-detection steps are inducible using SPBs of a defined mobility. For the practical realization of this sorting routine, the experiments have shed light on the impact of interparticle interactions. For the particle concentration used in the experiments presented in Fig. 2 and 3 of *ca.* 11 000 particles per  $\mu\text{L}$ , not all initially mobile SPBs could be transported back into the opposite direction after immobilization (see highlighted single SPBs in Fig. 2). The reason for this can be traced back to the interaction of an immobilized SPB with an incoming, movable SPB: the incoming bead may push the immobilized bead to an adjacent DW position with an even larger domain stripe width before the incoming bead itself eventually gets immobilized. As a result, the pushed bead may not be able to travel back into the opposite direction, as its transport step distance into the opposite direction is now larger than the transport step distance before the collision with the incoming bead. Conversely, SPBs may regain their mobility due to collision with approaching SPBs, which is occasionally observable in the intensity map of Fig. 3(a). This collision effect pronounces that the SPB concentration is another important factor for the fractionation efficiency when using specifically designed MFLs. This was verified by experimenting with a dramatically increased SPB concentration, where a large fraction of mobile beads was formed when using the same parameters for the external magnetic field sequence. Doing a simple calculation (see section S3 in the SI for details) based on particle size, minimum distance between single particles, and the extension of magnetophoretic separation areas on the substrate, we estimate a maximum Dynabeads M-270 concentration of *ca.* 1150 particles per  $\mu\text{L}$  for the here presented system to provide efficient SPB separation that is not influenced by particle collisions. Besides SPB concentration, slight fabrication-related deviations in the magnetic stray field landscape, the thickness of the deposited polymer spacer layer, or the homogeneity of the externally applied fields can cause different transport characteristics as well. However, by actuating several hundred particles per separation area simultaneously, the results presented in this work have a large statistical significance. The SPB fractionation is reproducible (especially the immobilization behavior for single SPBs not colliding with other particles) and can be improved by optimizing the magnetic domain pattern design as well as the particle concentration.



## 5 Conclusion

Parallel-stripe domains of gradually varied stripe width were imprinted into an EB thin film substrate to engineer a magnetic stray field landscape for the controlled spatial fractionation of liquid-dispersed SPBs transported close to the substrate surface. Ion bombardment induced magnetic patterning was employed to fabricate a *hh/tt* alternating magnetization configuration within the stripe domains, with the stripe width being periodically increased and decreased between 1.2  $\mu\text{m}$  and 10  $\mu\text{m}$ . The resulting MFL on top of the substrate leads to the capture and a stepwise, unidirectional transport of water-dispersed SPBs upon external application of a sequence of trapezoidal magnetic field pulses. SPBs with a diameter of 2.8  $\mu\text{m}$  were observed using an optical brightfield microscope to assemble in vertical rows on top of DW positions in the underlying substrate. Thus, the horizontal distance between adjacent SPB rows is locally different due to the gradually varied DW separation distance. Accordingly, the DW separation distance defines the transport step distance for one particular SPB row. Reaching the location of largest stripe domain width, SPBs transitioned to an oscillatory motion for a given configuration of external field pulses, resulting in their effective immobilization. Therefore, the SPB motion behavior is a function of lateral position, presuming a fixed frequency for the external field sequence. This is a significant advancement compared to established works, where the frequency of the external time-varying field needs to be tuned to initiate a transition from mobile to immobile SPBs. The locally different SPB motion regimes for our MFL design can be attributed to the lateral change in the transport step distance itself, as well as an observed decrease in SPB steady-state motion velocity with increasing transport step distance. While observing a spatial fractionation of nominally equal-sized SPBs due to statistical variations in their magnetophoretic mobility, a proof-of-concept experiment was finally conducted to deterministically fractionize SPBs of significantly different sizes. For this, a mixture of SPBs with diameters of 1.0  $\mu\text{m}$  and 2.8  $\mu\text{m}$  was placed on top of the substrate and all SPBs were transported to the largest stripe domains *via* an external field sequence of fixed frequency. After merely 3 s, all SPBs performed oscillatory motion but with a clear spatial distinction between 1.0  $\mu\text{m}$ - and 2.8  $\mu\text{m}$ -sized SPBs. Smaller SPBs were, on average, immobilized earlier (at smaller DW separation distance) than larger SPBs, leading to a significant spatial fractionation of both species. For collecting these particle fractions, a microfluidic channel structure can be integrated on top of the substrate surface. These channels would be placed parallel to the *y*-direction of the system (parallel to the stripe domain long axis), allowing for an externally applied fluid flow to push the separated SPB fractions into these channels and carry on with subsequent processes. Alternatively, the magnetic domain pattern may be modified to realize SPB transport in the *y*-direction as well, requiring a more intricate fabrication procedure.

Since the pattern of sequentially increasing/decreasing stripe domain width is periodically repeated throughout the whole substrate, the fractionation is parallelized for all on-chip present SPBs. This result may pave the way for high-throughput and time-efficient fractionation of magnetic particle species as a function of properties that are more difficult to disentangle, for instance, their surface characteristics. Since particles are transported in the vicinity of the substrate surface for our investigated system, changes in the surface properties lead to variations in the substrate surface-particle surface interaction. This, in turn, influences the separation distance between the two surfaces with an expected impact on the particle magnetophoretic mobility, *e.g.*, *via* the modified friction situation. Optimizing the MFL design for this functionality is one of our future tasks, rendering purpose-oriented MFLs as promising tools for the practical implementation of magnetic particle sorting routines in LOC devices.

## Author contributions

RH: conceptualization, investigation, formal analysis, visualization, writing – original draft. LP: investigation, formal analysis, writing – review & editing. PK: investigation, resources, writing – review & editing. AE: conceptualization, resources, supervision, project administration, funding acquisition, writing – review & editing.

## Conflicts of interest

There are no conflicts to declare.

## Data availability

Data for this article, including raw video recordings of magnetic particle motion, are available at DaKS – University of Kassel's research data repository at <https://doi.org/10.48662/daks-481>.

Supplementary information (SI): resist structure utilized for magnetic patterning, velocity during a transport step as a function of step distance for all observed particles, estimation of ideal particle concentration for efficient separation, and exemplary videos for particle motion. See DOI: <https://doi.org/10.1039/d5lc01000d>.

## Acknowledgements

RH, LP, and AE acknowledge project and scientific infrastructure funding by the German Research Foundation (DFG) under the project numbers 514858524, 433501699, 361379292, and 361396165. PK acknowledges financial support from the National Science Centre, Poland, under grant number 2020/39/B/ST5/01915. The authors acknowledge fruitful discussions with M. Vogel, Kiel University.



## References

- 1 L. J. Kricka, *Clin. Chim. Acta*, 2001, **307**, 219–223.
- 2 J. Knight, *Nature*, 2002, **418**, 474–475.
- 3 A. Manz, N. Gruber and H. M. Widmer, *Sens. Actuators, B*, 1990, **1**, 244–248.
- 4 A. K. Yetisen, M. S. Akram and C. R. Lowe, *Lab Chip*, 2013, **13**, 2210–2251.
- 5 S. Cardoso, D. C. Leitao, T. M. Dias, J. Valadeiro, M. D. Silva, A. Chicharo, V. Silverio, J. Gaspar and P. P. Freitas, *J. Phys. D: Appl. Phys.*, 2017, **50**, 213001.
- 6 Y. Zhang, X. Liu, L. Wang, H. Yang, X. Zhang, C. Zhu, W. Wang, L. Yan and B. Li, *Sci. Rep.*, 2020, **10**, 9604.
- 7 Q. A. Pankhurst, J. Connolly, S. K. Jones and J. Dobson, *J. Phys. D: Appl. Phys.*, 2003, **36**, R167–R181.
- 8 M. A. M. Gijs, *Microfluid. Nanofluid.*, 2004, **1**, 22–40.
- 9 N. Pamme, *Lab Chip*, 2006, **6**, 24–38.
- 10 C. Ruffert, *Micromachines*, 2016, **7**, 21.
- 11 Y. Gao, A. V. Reenen, M. A. Hulsen, A. M. D. Jong, M. W. Prins and J. M. D. Toonder, *Lab Chip*, 2013, **13**, 1394–1401.
- 12 C. P. Moerland, L. J. V. Ijzendoorn and M. W. Prins, *Lab Chip*, 2019, **19**, 919–933.
- 13 Y. F. Ran, C. Fields, J. Muzard, V. Liauchuk, M. Carr, W. Hall and G. U. Lee, *Analyst*, 2014, **139**, 6126–6134.
- 14 S. Rampini, P. Li, D. Gandhi, M. Mutas, Y. F. Ran, M. Carr and G. U. Lee, *Sci. Rep.*, 2021, **11**, 5302.
- 15 M. Reginka, H. Hoang, Ö. Efendi, M. Merkel, R. Huhnstock, D. Holzinger, K. Dingel, B. Sick, D. Bertinetti, F. W. Herberg and A. Ehresmann, *Langmuir*, 2021, **37**, 8498–8507.
- 16 N. Feely, A. Wdowicz, A. Chevalier, Y. Wang, P. Li, F. Rollo and G. U. Lee, *Small*, 2023, **19**, 2207154.
- 17 N. Wise, D. T. Grob, K. Morten, I. Thompson and S. Sheard, *J. Magn. Magn. Mater.*, 2015, **384**, 328–334.
- 18 C. Zhou, E. D. Boland, P. W. Todd and T. R. Hanley, *Cytometry, Part A*, 2016, **89**, 585–593.
- 19 M. Donolato, B. T. Dalslet and M. F. Hansen, *Biomicrofluidics*, 2012, **6**, 024110.
- 20 S. Rampini, P. Li and G. U. Lee, *Lab Chip*, 2016, **16**, 3645–3663.
- 21 F. Block, F. Klingbeil, U. Sajjad, C. Arndt, S. Sindt, D. Seidler, L. Thormählen, C. Selhuber-Unkel and J. McCord, *Adv. Mater. Technol.*, 2023, **8**, 2300260.
- 22 P. Tierno, F. Sagués, T. H. Johansen and T. M. Fischer, *Phys. Chem. Chem. Phys.*, 2009, **11**, 9615–9625.
- 23 D. Holzinger, I. Koch, S. Burgard and A. Ehresmann, *ACS Nano*, 2015, **9**, 7323–7331.
- 24 M. Urbaniak, D. Kiphart, M. Matczak, F. Stobiecki, G. D. Chaves-O'Flynn and P. Kuswik, *Sci. Rep.*, 2024, **14**, 23771.
- 25 B. B. Yellen, R. M. Erb, H. S. Son, R. Hewlin, H. Shang and G. U. Lee, *Lab Chip*, 2007, **7**, 1681–1688.
- 26 B. B. Yellen and L. N. Virgin, *Phys. Rev. E: Stat., Nonlinear, Soft Matter Phys.*, 2009, **80**, 011402.
- 27 R. Huhnstock, L. Paetzold, M. Merkel, P. Kuswik and A. Ehresmann, *Small*, 2024, **20**, 2305675.
- 28 H. Kim, A. Ali, Y. Kang, B. Lim and C. Kim, *ACS Appl. Mater. Interfaces*, 2025, **17**, 12772–12781.
- 29 R. Abedini-Nassab, M. A. Toosi, Y. Shen, F. Maghsoudi and Y. Dan, *IEEE Sens. J.*, 2025, **25**, 382–389.
- 30 C. Liu, L. Lagae, R. Wirix-Speetjens and G. Borghs, *J. Appl. Phys.*, 2007, **101**, 024913.
- 31 A. Mougin, S. Poppe, J. Fassbender, B. Hillebrands, G. Faini, U. Ebels, M. Jung, D. Engel, A. Ehresmann and H. Schmoranzer, *J. Appl. Phys.*, 2001, **89**, 6606–6608.
- 32 A. Ehresmann, I. Krug, A. Kronenberger, A. Ehlers and D. Engel, *J. Magn. Magn. Mater.*, 2004, **280**, 369–376.
- 33 A. Ehresmann, I. Koch and D. Holzinger, *Sensors*, 2015, **15**, 28854–28888.
- 34 D. Lengemann, D. Engel and A. Ehresmann, *Rev. Sci. Instrum.*, 2012, **83**, 53303.
- 35 A. Vansteenkiste, J. Leliaert, M. Dvornik, M. Helsen, F. Garcia-Sanchez and B. V. Waeyenberge, *AIP Adv.*, 2014, **4**, 107133.
- 36 D. V. Berkov, C. T. Boone and I. N. Krivorotov, *Phys. Rev. B: Condens. Matter Mater. Phys.*, 2011, **83**, 54420.
- 37 H. Huckfeldt, A. Gaul, N. D. Mügliche, D. Holzinger, D. Nissen, M. Albrecht, D. Emmrich, A. Beyer, A. Gölzhäuser and A. Ehresmann, *J. Phys.: Condens. Matter*, 2017, **29**, 125801.
- 38 D. Holzinger, N. Zingsem, I. Koch, A. Gaul, M. Fohler, C. Schmidt and A. Ehresmann, *J. Appl. Phys.*, 2013, **114**, 013908.
- 39 N. D. Mügliche, M. Merkel, A. Gaul, M. Meyl, G. Götz, G. Reiss, T. Kuschel and A. Ehresmann, *New J. Phys.*, 2018, **20**, 053018.
- 40 W. Nolting, *Grundkurs Theoretische Physik 3*, Springer, Berlin Heidelberg, 2013.
- 41 D. T. Grob, N. Wise, O. Oduwole and S. Sheard, *J. Magn. Magn. Mater.*, 2018, **452**, 134–140.
- 42 R. Wirix-Speetjens, W. Fyen, K. Xu, J. D. Boeck and G. Borghs, *IEEE Trans. Magn.*, 2005, **41**, 4128–4133.

